

Article

A Square Wave Alternating Current Preheating with High Applicability and Effectiveness of Preventing Lithium Plating

Guanlin Liu ^{1,†}, Zeping Zhang ^{2,*}, Jinke Gong ², Qiong Li ¹, Yun Zhou ¹ and Hongfu Zou ¹¹ College of Automotive Engineering, Hunan Industry Polytechnic, Changsha 410208, China² College of Mechanical and Vehicle Engineering, Hunan University, Changsha 410082, China

* Correspondence: hnuweiming@gmail.com

† These authors contributed equally to this work.

Abstract: Alternating current preheating (ACP) of lithium-ion batteries has the advantage of a high heating rate while inhibiting lithium plating. Two strategies based on terminal voltage control and full battery impedance control were proposed to simplify the ACP implementation. However, such strategies either severely compromise the preheating rate or induce non-negligible lithium plating. To maximize the preheating rate while ensuring no lithium plating, an ACP method based on anode potential control is developed using a square wave alternating current. The operation boundaries of lithium plating prevention, in terms of frequency and maximum permissible current amplitude, are determined using the anode potential and impedance. Their effectiveness in preventing lithium plating is validated by repeating 800 cycles of preheating. By applying the operation boundaries, a temperature-adaptive preheating is found to be able to speed up the preheating rate with higher frequency, smaller temperature intervals and better thermal insulation. When the battery is preheated at a frequency of 400 Hz, with a temperature interval of 5 °C and a heat transfer coefficient of 5 Wm⁻² K⁻¹, the preheating rate can reach 6.61 °C/min, exceeding the method based on the terminal voltage control by 5.4%, and larger than that based on the full battery impedance control strategy by 41.8%.

Keywords: alternating current preheating; square wave; lithium-plating; temperature-adaptive

Citation: Liu, G.; Zhang, Z.; Gong, J.; Li, Q.; Zhou, Y.; Zou, H. A Square Wave Alternating Current Preheating with High Applicability and Effectiveness of Preventing Lithium Plating. *Processes* **2023**, *11*, 1089. <https://doi.org/10.3390/pr11041089>

Academic Editor: Qunjie Xu

Received: 9 January 2023

Revised: 23 March 2023

Accepted: 28 March 2023

Published: 4 April 2023



Copyright: © 2023 by the authors. Licensee MDPI, Basel, Switzerland. This article is an open access article distributed under the terms and conditions of the Creative Commons Attribution (CC BY) license (<https://creativecommons.org/licenses/by/4.0/>).

1. Introduction

Lithium-ion batteries (LIBs) have been extensively implemented in the industry of electric vehicles and energy storage due to their high energy/power density, long lifetime and low self-discharge rate. The impedance of LIBs with graphite negative electrodes increases drastically in cold environments, sharply decreasing the discharge power and available energy [1]. In addition, low-temperature operation may induce the Li-ion plating in-between the graphite particles and electrolytes, resulting in battery degradation and even safety hazards [2]. Therefore, heating up LIBs to a suitable temperature range (such as 0 °C or 5 °C) before usage is pragmatically required at low temperatures.

To strengthen the low-temperature performance of LIBs, external and internal preheating methods are usually adopted. For external preheating methods, various heat actuators are generally used to heat the batteries through convection or conduction [3–5]. However, related methods are considered to be inefficient due to the long heat transfer path and high thermal resistance in between components. Contrarily, internal preheating methods, generally warming up the batteries themselves using the heat produced by their internal resistances, removes the process of heat conduction, exhibiting higher rates and better temperature uniformity.

Alternating current preheating (ACP) has drawn a lot of attention among internal preheating methods due to its high preheating rate and capability to prevent lithium plating. Zhang et al. [6] developed an internal preheating method for LIBs using sinusoidal

alternating current (SAC). Based on an equivalent electrical circuit (EEC) model, a heat generation model in the frequency domain was proposed so as to predict the battery temperature evolution during the ACP. Utilizing the method, an 18,650 battery was warmed up from $-20\text{ }^{\circ}\text{C}$ to $5\text{ }^{\circ}\text{C}$ within 15 min. Zhu et al. [7] examined the temperature distribution on a LiFePO_4/C battery with a large capacity by adjusting the amplitude and frequency of alternating current. The maximum temperature difference on the battery surface is no higher than $2\text{ }^{\circ}\text{C}$ in the test using the external alternating current excitation with an amplitude of 1.25 C and at a frequency of 1 Hz. Regarding the implementation of the ACP method, hardware circuits, including a soft-switching circuit [8], buck–boost conversion [9], and drive circuitry of an electric vehicle [10], have been designed to preheat the signal battery or battery module.

A key concern about the ACP method is the risk of lithium plating when the battery is forcefully charged at low temperatures. According to the Li plating mechanism, the anode potential criterion that the sum of the negative electrode equilibrium potential (U_e) at a given state of charge (SOC) and over-potential of the negative electrode (η) shall be above 0, i.e., $U_e + \eta > 0$, is widely introduced in the previous studies to develop the preheating strategies of lithium-plating-prevention [8,11,12].

Based on the anode potential control and negative electrode impedance, Ge et al. [11] proposed a lithium-plating-free ACP method in the scenario of using SAC. The current limiting curves, capable of inhabiting lithium plating, are also provided at different temperatures. Integrating the current limiting curves with their proposed heat generation rate model, a multistep ACP method has been developed, successfully warming up a laminated Li-ion battery from $-20\text{ }^{\circ}\text{C}$ to $5\text{ }^{\circ}\text{C}$ in 800 s. However, the method demands the anode potential and negative electrode impedance, which rely on the implementation of a three-electrode battery.

To simplify the implementation of ACP, two full-battery-based strategies based on full battery impedance control and terminal voltage control have been extensively adopted by limiting the full battery reaction overpotential [8,12] or keeping the maximum polarization voltage of a full battery constant [13–15].

As for the first strategy, replacing negative electrode impedance using full battery impedance is generally adopted according to some electrochemical impedance spectroscopy (EIS) results showing that the charge transfer impedance derived from the negative electrode (NR_{ct}) is much larger than that from the positive electrode (PR_{ct}) [11]. However, the result lacks general applicability for different batteries and at different temperatures. As for the cases with the PR_{ct} close to the NR_{ct} , such a strategy can tighten up the maximum permissible amplitudes of the lithium plating prevention and reserve excessive parameter redundancy, resulting in the severe depression of the preheating rate [16]. In addition, the strategy evades the issue of obtaining the negative electrode equilibrium potential by referring to existing results [12] or neglecting U_e via directly making $\eta > 0$ [8].

As for the second strategy, Ruan et al. [13] proposed an ACP method with overvoltage $\leq 0.5\text{ V}$ or $\geq 0.5\text{ V}$ to achieve a good balance between the heating time and the battery lifespan. Zhu et al. [7,14] developed an alternating current pulse heating approach by adjusting the current parameters to warrant the terminal voltage of the battery within the working voltage range. Despite the fact that the related works achieved a fast and lithium-plating-free preheating, the principle of setting the voltage threshold lacks a solid theoretical basis. Fundamentally, this strategy cannot distinguish the anode potential and cathode potential. The anode potential criterion for preventing lithium plating may not be precisely guaranteed, e.g., the strategy is found to induce lithium plating at low frequencies in work [16], or may be overly limited by controlling the terminal voltage, e.g., when open circuit voltage (OCV) is close to the upper or lower voltage limitation of the battery.

In summary, among the above three kinds of ACP, the method based on the anode potential control and negative electrode impedance is the most scientific and accurate for preventing lithium plating, despite the fact that it requires a reference electrode. Actually, as regards its application in real situations, calibrating the maximum permissible current

parameters in the development phase and looking up a table in the usage phase is a feasible and commonly-used-in-engineering strategy. In addition, combined with the state of health estimation methods, this kind of ACP method can be further optimized when considering battery inconsistency and battery aging. Moreover, due to the advantages of in-situ monitoring and characterizing the electrochemical performance of electrodes, the reference electrode configuration has aroused many battery manufacturer's interests to embed it in commercial LIB [17,18]. Although the present LIBs have not equipped reference electrodes, several patents have reported the implementation of the reference electrodes in practical rechargeable batteries [19–23]. The researchers of [24] also declared a remarkable breakthrough in improving the lifetime and accuracy of the three-electrode battery. The lifetime of their developed three-electrode battery has exceeded 500 h, already having the potential for application in real situations. Consequently, the ACP approach based on the anode potential criterion shall be an applicable and promising technology and herein is employed to acquire the operation boundaries of preventing lithium plating in terms of current amplitude and frequency.

The waveform of the alternating current is another crucial issue in the implementation of the ACP method. In previous papers, the alternating current with sinusoidal waves has been widely adopted. However, it is very difficult to generate in the case of electric vehicles or chargers. Furthermore, the sinusoidal wave current may suppress the heating efficiency due to its low energy flux density. Consequently, searching for an applicable waveform with high efficiency is urgent. Since the square wave alternating current (SWAC) can be easier to generate through switching devices and carries higher energy flux density, it shows higher potential to apply in real situations. Although several works have investigated the effect of a square wave current or likewise on preheating performance [7,12,25,26], most works adapt full-battery-based strategies, and few have provided the deterministic and intrinsic operation boundaries of lithium plating prevention and fully released the preheating capability of ACP using the SWAC excitation.

In this paper, we develop a rapid and lithium-plating-free ACP approach using the excitation of SWAC. A heat generation model in the frequency domain is established based on the EEC model. The impact of current parameters, including frequency, amplitude and waveform, on the preheating rate is experimentally investigated. Operation boundaries of lithium plating prevention are determined using the fitted EEC parameters of negative electrode EIS and the lithium plating potential. The effectiveness of operation boundaries, together with their effect on battery health, is explored through the aging tests. By combining the operation boundaries and the ACP method with SWAC, a temperature-adaptive procedure with different frequencies, temperature intervals and heat transfer coefficients is explored. The procedure is found to be able to significantly speed up the preheating rate with higher frequency, smaller temperature intervals, and better thermal insulation. In addition, the proposed method in this paper is evaluated in terms of preheating rate by comparing it with the preheating methods based on the two full-battery-based strategies. The results demonstrate that the proposed method has more robust strength than these using the full-battery-based strategies at high frequency.

The rest of this paper is organized as follows. The theoretical considerations about heat generation and Li-ion plating prevention are introduced in Section 2. The experimental setups are presented in Section 3. The model validation, operation boundaries of lithium plating prevention and temperature-adaptive preheating are discussed in Section 4. Finally, conclusions are summarized in Section 5.

2. Theoretical Considerations

2.1. Temperature Rising Model for ACP with SWAC

The Bernardi equation is widely used to estimate the heat generation of LIBs [27,28]. Neglecting the enthalpy of mixing and the heat of phase change, the equation is simplified as,

$$q = I(U_{oc} - V) - IT \frac{\partial U_{oc}}{\partial T} \quad (1)$$

where $\frac{\partial U_{oc}}{\partial T}$ is the entropy coefficient, and I is assumed to be positive during charge. The first term on the right side of Equation (1) denotes the irreversible heat. The second denotes the reversible heat, which can be canceled out as the battery is subject to a symmetrical alternating current.

As for a battery excited by the SAC, as shown in Equation (2), the terminal voltage response can be expressed as Equation (3).

$$i(t) = I_{ac}^{SAC} \sin(\omega t) \quad (2)$$

$$V(t) = U_{oc} + V_{ac}^{SAC} \sin(\omega t + \varphi) \quad (3)$$

Combining Equations (1)–(3), the heat generation of the battery is expressed as,

$$q(t) = -I_{ac}^{SAC} T \frac{\partial U_{oc}}{\partial T} \sin(\omega t) + \frac{I_{ac}^{SAC} V_{ac}^{SAC}}{2} \cos(\varphi) - \frac{I_{ac}^{SAC} V_{ac}^{SAC}}{2} \cos(2\omega t + \varphi) \quad (4)$$

where both the first term and the third term are the trigonometric function of time t . Their time integrals can be seen as 0 in the long run. Therefore, the battery's average heat generation rate q_{SAC} in a period can be expressed as,

$$q_{SAC} = \frac{1}{2} (I_{ac}^{SAC})^2 Z_{Re} \quad (5)$$

where Z_{Re} is the real part of the impedance of the EEC, as shown in Figure 1, which includes the ohmic resistance (Z_1), the solid electrolyte interphase (SEI) resistance (Z_2), the charge transfer resistance at the interface of solid–liquid phase, and the transport resistance of Li^+ in solid and liquid phases (Z_3). In the EEC model, C_{SEI} and C_{dl} represent the constant phase element (CPE) of SEI and the electrical double layer, respectively. From the EEC model, the real part of the impedance of the lithium battery is calculated as,

$$Z_{Re}(\omega) = R_0 + \frac{1 + R_{SEI} Q_{SEI} \omega^{n_{SEI}} \cos(\frac{n_{SEI}\pi}{2})}{1 + 2R_{SEI} Q_{SEI} \omega^{n_{SEI}} \cos(\frac{n_{SEI}\pi}{2}) + (R_{SEI} Q_{SEI} \omega^{n_{SEI}})^2} R_{SEI} + \frac{1 + R_{ct} Q_{dl} \omega^{n_{dl}} \cos(\frac{n_{dl}\pi}{2})}{1 + 2R_{ct} Q_{dl} \omega^{n_{dl}} \cos(\frac{n_{dl}\pi}{2}) + (R_{ct} Q_{dl} \omega^{n_{dl}})^2} R_{ct} \quad (6)$$

where Q_{SEI} and n_{SEI} are the coefficient and exponent of C_{SEI} , and Q_{dl} and n_{dl} are the coefficient and exponent of C_{dl} . For the components in EEC, Q_{SEI} , Q_{dl} , R_{SEI} and R_{ct} are functions of SOC, temperature (T), and current frequency (f), R_0 is a function of the SOC, and temperature is (T).

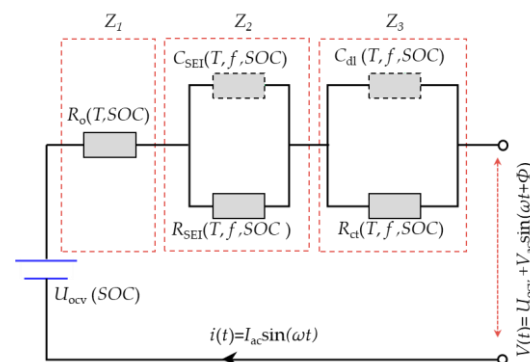


Figure 1. Equivalent electrical circuit (EEC) model.

In order to extend the heat generation rate model, as shown in Equation (5), to the scenario of using SWAC excitation, the SWAC with a period of A , as shown in Equation (7), is

converted to a superimposition of 128 sinusoidal alternating currents by Fourier transform, as expressed in Equation (8).

$$i(t) = \begin{cases} -I_{ac}^{SWAC} & (-\frac{A}{2} < t < 0) \\ I_{ac}^{SWAC} & (0 < t < \frac{A}{2}) \end{cases} \quad (7)$$

$$i(t) = \frac{4}{\pi} \sum_{n=1}^{128} \frac{I_{ac}^{SWAC}}{2n-1} \sin((2n-1)\omega t) \quad (8)$$

where $\omega = 2\pi/A$ is the angular frequency of the SWAC.

Combining Equations (5), (6), and (8), the heat generation rate of using SWAC q_{SWAC} is expressed by,

$$q_{SWAC} = \frac{8}{\pi^2} \sum_{n=1}^{128} \left(\frac{I_{ac}^{SWAC}}{2n-1} \right)^2 Z_{Re}((2n-1)\omega) \quad (9)$$

Considering the temperature difference between the external and the internal of a prismatic battery is less than 2 °C, even if the battery is charged at 2C [29], a lumped model is herein utilized to express the temperature variation of the battery,

$$mc \frac{dT}{dt} = q_{SWAC} - hS(T - T_{amb}) \quad (10)$$

2.2. Analysis on Preventing Li-Ion Plating

Li^+ is prone to plating on the graphite particles in subzero environments when the potential difference between the solid and electrolyte phase in the anode electrode is less than the reaction potential of lithium plating [30,31],

$$\phi_s - \phi_l > E_{Li/Li^+} \quad (11)$$

where E_{Li/Li^+} is the reaction potential of Li plating, which is usually seen as 0 V vs. Li/Li^+ [31,32].

When the lithium plating occurs in between the surface of the graphite particle and SEI, the negative electrode overpotential η_n equals [32],

$$\eta = \phi_s - \phi_l - U_e \quad (12)$$

where the value of U_e at the different SOC can be measured using the three-electrode battery, as presented in Figure 2. In this paper, the value of U_e at the 50% SOC equals 0.1354 V.

Combining Equations (11) and (12), the over-potential of the negative electrode to prevent lithium plating during the charging period is required as,

$$\eta + U_e = \phi_s - \phi_l > 0 \quad (13)$$

$$|\eta| < U_e \quad (14)$$

Linearizing the Butler–Volmer equation [33], the over-potential approximately equals

$$|\eta| \approx i_{ct} \cdot R_{ct} \quad (15)$$

Applying Equation (15) to the EEC model of the negative electrode,

$$i_{ct} \cdot R_{ct} = V_3^{neg} = i \cdot Z_3^{neg} \quad (16)$$

Combining Equations (14) and (16), the criterion of preventing the Li-ion plating in the preheating process with SWAC excitation can be expressed as,

$$|V_3^{\text{neg}}| = I_{\text{ac}} \cdot |Z_3^{\text{neg}}| \leq U_e \quad (17)$$

where $|V_3^{\text{neg}}|$ is the amplitude of the voltage across the Z_3 part of the EEC of the negative electrode, the Z_3^{neg} impedance can be expressed by,

$$Z_3^{\text{neg}}(\omega) = \frac{R_{\text{ct}}^{\text{neg}}}{(j\omega)^{n_{\text{dl}}^{\text{neg}}} Q_{\text{dl}}^{\text{neg}} R_{\text{ct}}^{\text{neg}} + 1} \quad (18)$$

As for the scenario of SWAC, the maximum permissible amplitude I_{SWAC} of preventing lithium plating can be obtained by combining Equations (8) and (17) and is expressed as,

$$\frac{4}{\pi} \left| \sum_{n=1}^{128} U_n^{\text{neg}} \right| \leq U_e \quad (19)$$

where $U_n^{\text{neg}} = \frac{I_{\text{SWAC}}}{2n-1} \sin((2n-1)\omega t + \varphi_n^{\text{neg}}) \cdot Z_3^{\text{neg}}((2n-1)\omega)$; $\varphi_n^{\text{neg}} = \arctan\left(\frac{\text{Re}(Z_3^{\text{neg}}((2n-1)\omega))}{\text{Im}(Z_3^{\text{neg}}((2n-1)\omega))}\right)$; $n = (1, 2, \dots, 128)$.

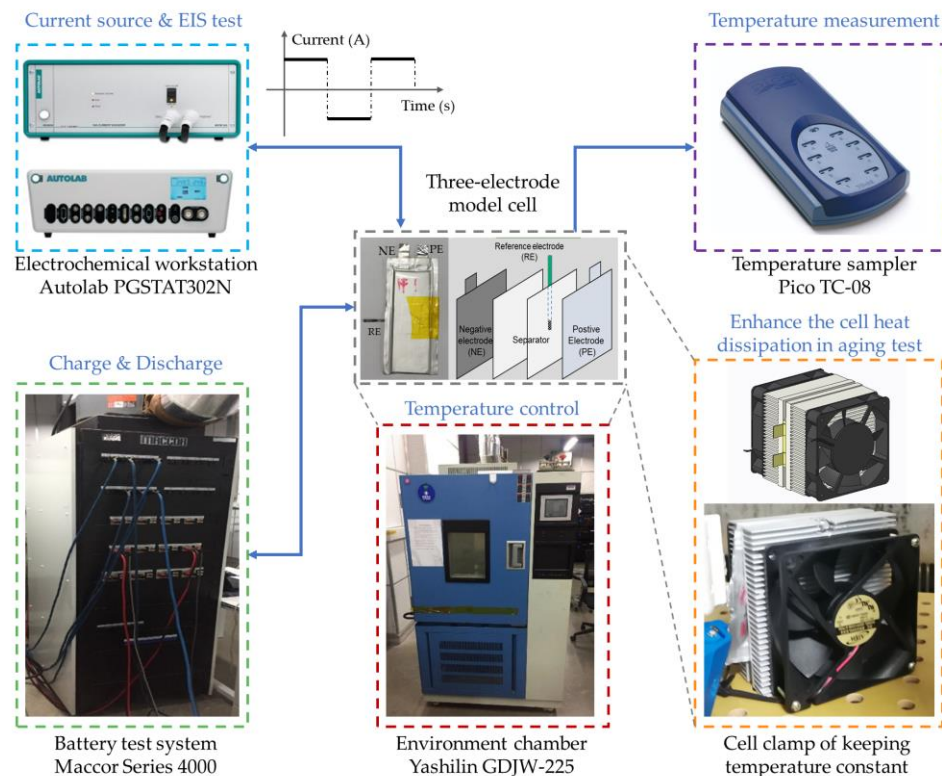


Figure 2. The experimental platform for EIS and preheating tests.

3. Experiment

The batteries used in this paper are the laminated three-electrode model batteries. The specifications of the test batteries are presented in Table 1. A copper wire with 100 μm diameter was used as the reference electrode. Li was deposited at the end of copper wire and with a length of 1 cm to provide a reference potential of Li/Li^+ . The schematic of the three-electrode battery is presented in Figure 2. The reference electrode was activated using the method in Ref. [34]. The model batteries were cycled 3 times with a current of 0.05 C

at 25 °C so as to stabilize the three-electrode battery. The effectiveness of the reference electrode is validated in Supplementary Material (SM) Figure S1.

Table 1. Specifications of the test batteries.

Item	Values
Battery type	Laminated lithium-ion model battery
Anode	Graphite
Cathode	$\text{LiNi}_{1/3}\text{Co}_{1/3}\text{Mn}_{1/3}\text{O}_2$
Electrolyte	LiPF_6 in organic solvent
Reference electrode	Li metal deposited on copper wire (100 μm)
Battery mass	56 g
Length and width	117 mm and 43 mm
Specific heat capacity	$1.24 \text{ Jg}^{-1} \text{ K}^{-1}$
SOC	50%
Capacity	3.1 Ah

The experimental platform in this paper is depicted in Figure 2, comprising a testing system and a data acquisition system. In the platform, an electrochemical workstation (Autolab PGSTAT302N) was used to carry out EIS tests and as a current source for preheating experiments. A climate chamber (GDJW-225) was used to provide a manageable temperature, and a battery charging/discharging system (Maccor Series 4000) was used to assess battery degradation. The data acquisition system comprises a temperature sample device (Pico TC-08) and an electric signal acquisition unit for the battery charging/discharging system. A battery clamp was designed to enhance the battery heat dissipation so as to make the battery temperature equal to the set chamber temperature in aging tests as follows. The details of the tests are shown in Table 2.

Table 2. The details of the tests.

Test	Item	Value
EIS tests	SOC	50%
	Battery temperature	$-20\text{ }^\circ\text{C}$, $-15\text{ }^\circ\text{C}$, $-10\text{ }^\circ\text{C}$, $-5\text{ }^\circ\text{C}$, $0\text{ }^\circ\text{C}$, $5\text{ }^\circ\text{C}$, $15\text{ }^\circ\text{C}$, $25\text{ }^\circ\text{C}$
Preheating tests	Current parameters	SWAC/SAC: 0.1 Hz 3 A, 0.1 Hz 5 A, 1 Hz 5 A
	Thermal insulation condition	The experimental battery was laid in a foam box; the calibrated coefficients of heat transfer in different temperature ranges are presented in the Supplementary Figure S2
Repeated preheating tests	SOC	50%
	Battery temperature	$-20\text{ }^\circ\text{C}$
	Control parameters	SWAC: the frequency is set to 50 Hz; the amplitude is plotted in Figure 7
Aging tests	Battery temperature	$25\text{ }^\circ\text{C}$
	Performance tests	Profile refers to the paper [6], the discharge rate adopts C/2
	RPT	
	ICA	1/25 C discharge until 2.5 V

3.1. EIS Measurement

Both the heat generation rate and the operation boundaries of Li plating prevention demand EEC parameters, which need to fit according to the EIS results. The EIS of the batteries were measured using an electrochemical workstation (Autolab PGSTAT302N). Before EIS, the SOCs of batteries were adjusted to 50% at room temperature with a current of 0.3 C and soaked at the fixed environment in the chamber (GDJW-225) for 3 h to stabilize the battery temperature. The potentiostatic excitation was selected with the amplitude of 5 mV over the frequency range of 10^4 – 10^{-2} Hz (61 data points). The EEC parameters were fitted utilizing the ZSimpWin software.

3.2. The Preheating Tests

To verify the effectiveness of the proposed temperature rising model and evaluate the preheating rate of ACP with SWAC, different sets of operating parameters were adopted to preheat the battery. In addition, alternating current with square and sinusoidal waveforms was used to investigate their influence on the temperature rising rate. The operating parameters are presented in Table 2. The alternating current was generated via an electrochemical workstation. The battery temperature was monitored by temperature sample equipment (Pico TC-08) with three T-type thermocouples. In the tests, once the battery temperature reached 5 °C or the preheating time exceeded 30 min, the preheating current was cut off. The cooling curve of the battery temperature was continuously recorded until it remained unchanged so as to calibrate the equivalent heat transfer coefficient in different temperature ranges. The calibrated result is presented in Supplementary Figure S2. In addition, before each test, the temperatures of batteries were stabilized at set values for 3 h.

3.3. Aging Tests with Square Wave Alternating Current

To validate the proposed operation boundary of preventing lithium plating, aging tests were performed on another two model batteries using the operating parameters, as presented in Table 2. In the tests, the temperature of the battery shall be kept at a fixed temperature so as to remove the interference of the boundary change induced by the temperature rise. To achieve this goal, a battery clamp is designed to make the heat dissipation larger than the heat generation. The schematic of the battery clamp is presented in Figure 2, where two heat sink fins are symmetrically placed on both sides of the tested batteries. Two cooling fans are fixed on the heat sink fins, respectively, so as to timely pump the heat away, making the battery temperature equal to the set chamber temperature. To explore the influence of square wave preheating upon battery health, performance tests, including a reference performance test (RPT) and an incremental capacity analysis (ICA), were carried out every 100 cycles of preheating (every 15 min preheating denotes one cycle). The operation parameters are shown in Table 2.

4. Results and Discussions

4.1. EIS Results and EEC Fitted Parameters

To identify the EEC parameters, the EIS of the model battery was measured at different temperatures. Figure 3a,b exhibits the EIS of a negative electrode and positive electrode relative to the reference electrode, and Figure 3c exhibits the EIS results of the full battery. As for each electrode, the EIS shows an increasing size at lower temperatures, which implies a significant increase in battery impedance at lower temperatures. The spectrum at lower temperatures moves towards the right side, indicating an increase in ohmic resistance with decreasing of temperature. In addition, structural changes can be observed when comparing EIS results at different temperatures. For instance, the oblique line in the low-frequency range, representing the Li⁺ diffusion process, gradually disappears with the decrease in temperature since the characteristic frequency of diffusion process exceeds the preset frequency range. In addition, by comparing the EIS of negative and positive electrodes, the impedance of the negative electrode shows a larger value than that of the positive at lower temperatures.

Figure 3d shows the proportion K of the negative electrode impedance to the full battery impedance at different frequencies and temperatures. As shown in the figure, the proportion K varies a lot at different temperatures and frequencies. On the whole, the proportion of the negative electrode impedance is larger at low temperatures and low frequencies. However, the proportion K decreases severely when increasing the frequency. The proportion K can decrease to 50% as the frequency is larger than 100 Hz. The significant variation of K indicates the strategy of replacing the negative impedance using the full battery impedance lacks general applicability at different temperatures and frequencies.

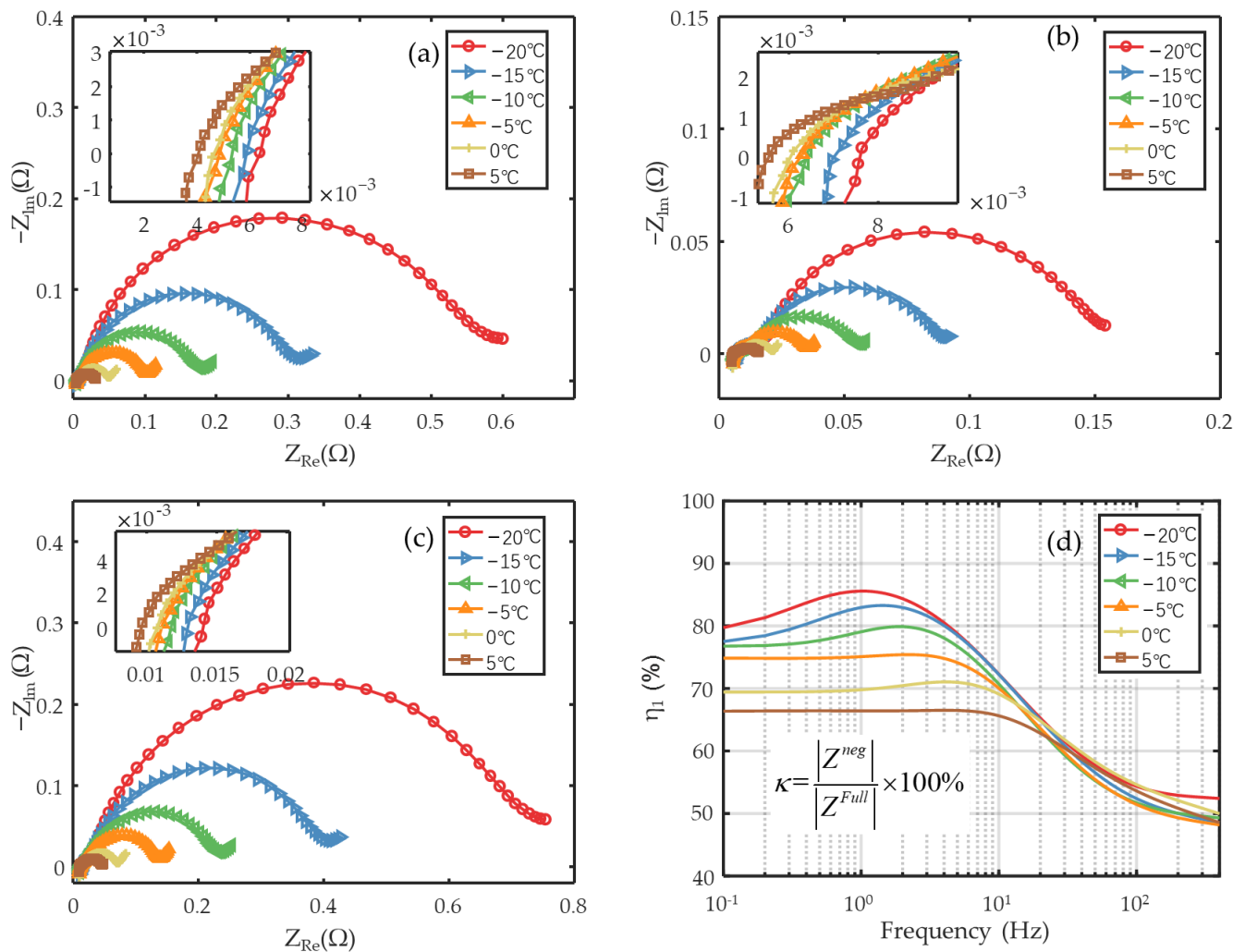


Figure 3. EIS results at different temperatures: (a) EIS of negative electrode; (b) EIS of positive electrode; (c) EIS results of full battery; (d) the proportion K of the negative electrode impedance to the full battery impedance.

Figure 4a–c present the EEC fitting results. Similar to the EIS results, the ohmic resistance R_o , the SEI film resistance R_{SEI} and the charge transfer resistance R_{ct} increase a lot with decreasing the temperature. Especially for R_{ct} , the variation is more pronounced than the R_o and R_{SEI} . In addition, compared with the resistances of positive electrodes, the resistances of negative electrodes change more severely, particularly when the temperature is less than -5°C . As for the Q_{SEI} , Q_{ct} , n_{SEI} and n_{ct} , the values and variation in the negative electrode are close to that of the full battery. It indicates that the performance of the full battery resembles that of the negative electrode when the temperature is lower than -5°C .

As depicted in Figure 4d, the R_{ct} increases significantly at low temperatures while following the Arrhenius equation with the battery temperature. Referring to Equation (1) in Ref [35], the activation energy of the charge transfer can be fitted. The fitted activation energy for the charge transfer of a negative electrode is 76.8 kJ mol^{-1} , a positive electrode, 81.9 kJ mol^{-1} , and the full battery, 75.9 kJ mol^{-1} . Such results indicate the R_{ct} of the positive electrode will be subject to a larger change in temperature evolution than that of negative electrode, leading to a decrease of the proportion of the negative electrode impedance to the full battery impedance at higher temperatures.

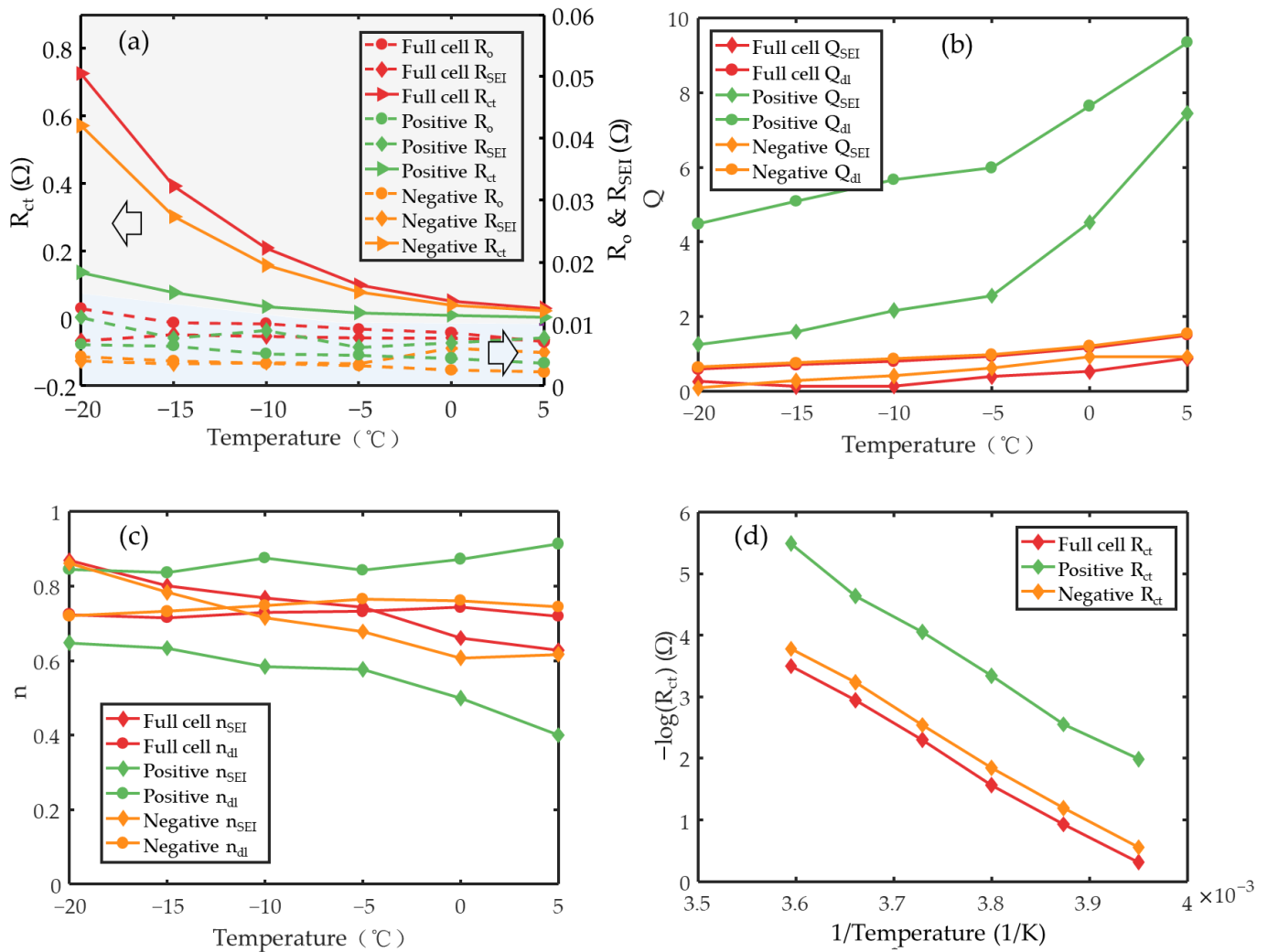


Figure 4. EEC fitted parameters: (a) Resistances; (b) coefficient of CPE, Q ; (c) exponent of CPE, n ; (d) Arrhenius plot of R_{ct} .

4.2. Model Validation and Preheating Performance

To verify the temperature rising model and evaluate the heating rate, the temperature variation of the model battery preheated using different operating parameters is investigated. The experimental and simulated temperature rising curves are presented in Figure 5a. High agreement between the model prediction and experimental result is presented. The maximum aberration, occurring at 5 A and 1 Hz, is about 1.2°C . The results demonstrate that the developed model is capable of predicting the temperature rise of the battery with high accuracy. In addition, the preheating rate becomes more effective when the frequency decreases and the current amplitude increases. In addition, the temperature evolution of the battery preheated using alternating current with a square and sinusoidal waveforms is experimentally investigated, and the result is presented in Figure 5b. A larger temperature rising rate is acquired for the battery heated up using SWAC. For example, the battery, heated by SWAC with the amplitude of 5 A and at the frequency of 1 Hz, can be warmed up from -20°C to -5.3°C within 800 s. The average temperature rising rate reaches $1.12^{\circ}\text{C}/\text{min}$. While for the battery heated by SAC with identical current parameters and at the same thermal insulation conditions, the average rate just reaches $0.75^{\circ}\text{C}/\text{min}$, with the temperature rising from -20°C to -9.8°C . Such results demonstrate a larger heating capability of ACP using SWAC than using SAC.

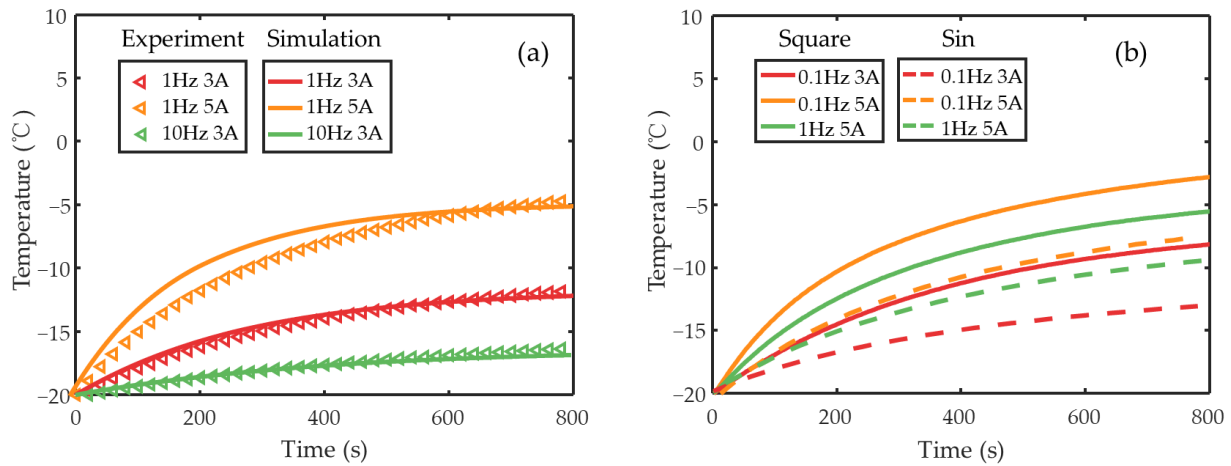


Figure 5. (a) Experimental and simulation results of preheating with SWAC; (b) experimental temperature evolution of the battery heated by alternating current with square and sinusoidal waveform.

4.3. Lithium Plating Prevention for SWAC

4.3.1. The Operation Boundaries of Lithium Plating Prevention for SWAC

When a battery is preheated using the SWAC with inappropriate operation parameters, a lithium ion may deposit on the surface of the negative electrode during the charging period. To effectively prevent the lithium plating, appropriate operation parameters of frequency and maximum permissible current amplitude are needed for engineers to formulate the preheating strategy. Through Equation (19), the operation boundaries of lithium plating prevention are calculated using the fitted EEC parameters of the negative electrode for ACP with SWAC. The results are presented in Figure 6a.

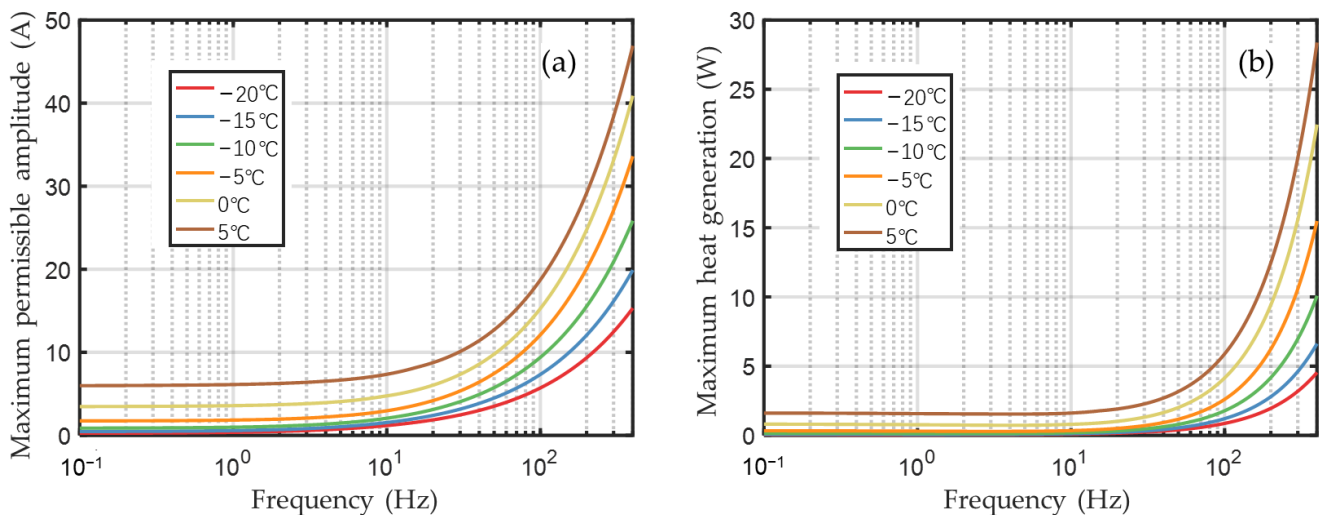


Figure 6. (a) Operation boundaries of lithium plating prevention in terms of maximum current amplitudes at different frequencies and different temperatures; (b) maximum heat generation rate at different frequencies and different temperatures.

In the figure, the maximum permissible amplitude reduces a lot with decreasing temperature and rises significantly with increasing frequency. The results are mainly due to the property of large R_{ct} at low temperatures, as well as the characteristic of the quick decrease in $|Z_3|$ at high frequencies. Integrating the heat generation model with the operation boundaries, the maximum heat generation rate of the battery is calculated by Equation (9) by accounting for the irreversible heat generated in the positive electrode and

negative electrode. The results are exhibited in Figure 6b. Despite the fact that the real part of the impedance decreases a lot at higher temperatures and larger frequencies, the maximum heat generation rate still increases at higher frequencies and temperatures. The reason for such a result is that the heat generation rate is proportional to the square of the current amplitude, as shown in Equation (9).

4.3.2. The Validation of the Operation Boundary of Lithium Plating Prevention

To validate the operation boundary of lithium plating prevention, two model batteries with high consistency were repeatedly preheated at $-20\text{ }^{\circ}\text{C}$. The adopted current parameters, together with the operation boundary at $-20\text{ }^{\circ}\text{C}$, are presented in Figure 7a. The point on the red curve denotes the adopted amplitude of battery A, the point out of the red curve denotes the adopted amplitude of battery B, and the amplitude of battery B is larger than that of Battery A by 15%. The temperature batteries were stabilized at $-20\text{ }^{\circ}\text{C}$ using the battery clamp. The battery temperature evolution during the aging test is presented in Figure 7b and denoted by the red curve. As shown in the figure, the battery is stably maintained at $-20\text{ }^{\circ}\text{C}$. The temperature fluctuation at the beginning is negligible when compared with the 100 cycles of repeated preheating (1500 min).

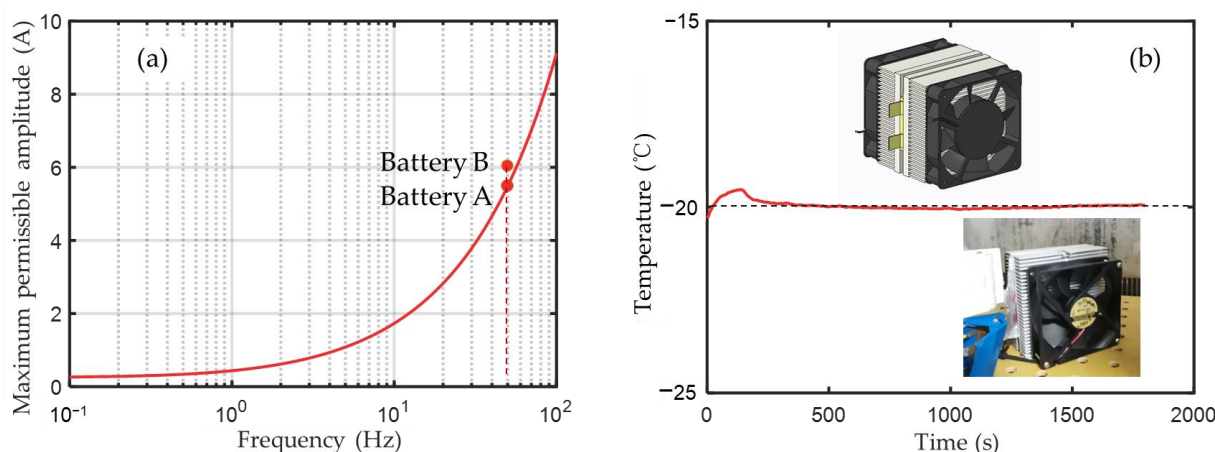


Figure 7. (a) The current parameters adopted in aging tests; (b) the battery temperature evolution during the repeated preheating, as well as the battery clamp.

To probe the condition of lithium plating on graphite electrode, the techniques of scanning electron microscope (SEM) and energy-dispersive x-ray spectroscopy (EDS) were implemented upon the disassembled batteries, which are repeatedly preheated for 800 cycles. The SEM images are depicted in Figure 8, and the EDS results are depicted in Figure 9.

As for the SEM images of battery A, as presented in Figure 8a1–a3, typical graphite morphology is clearly exposed. Neither the dendritic morphology nor the mossy morphology is observed in the SEM images of the negative electrode. In contrast, lithium dendrite is noticeably observed on the surface of the negative electrode of battery B. The results validate the effectiveness of the operation boundary of lithium plating prevention well.

The lithium plating can be determined by the weight of oxygen (O) in elementary components of the negative electrode as well since the plating can introduce extra O due to the oxidized lithium metal in the transfer process. As presented in Figure 9(c1,c2), the weight of the O in battery A only accounts for 4.3%, while the weight of the O in battery B severely increases to 51.68%. The pronounced increase in the weight of the O also indicates the occurrence of lithium plating on the graphite electrode of battery B. Of note, the small weight of the O in battery A, together with fluorine (F) and phosphorus (P) in both battery A and battery B, is mainly from the components of the SEI and electrolyte left on the surface of the graphite electrode. The carbon (C) chiefly derives from the graphite matrix.

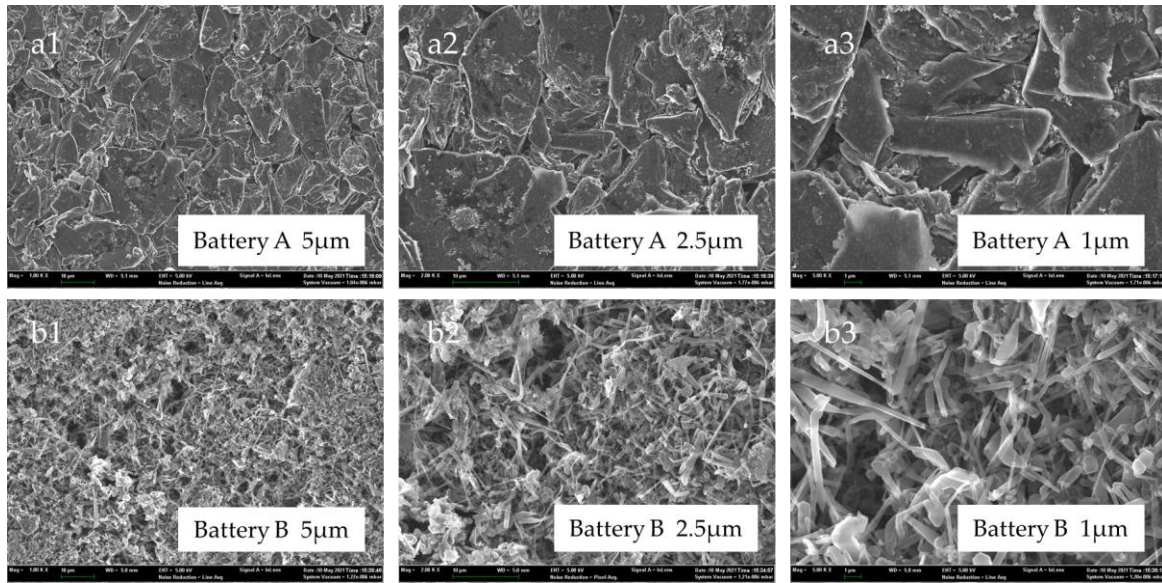


Figure 8. The SEM images of the negative electrode: (a1–a3) Battery A; (b1–b3) Battery B.

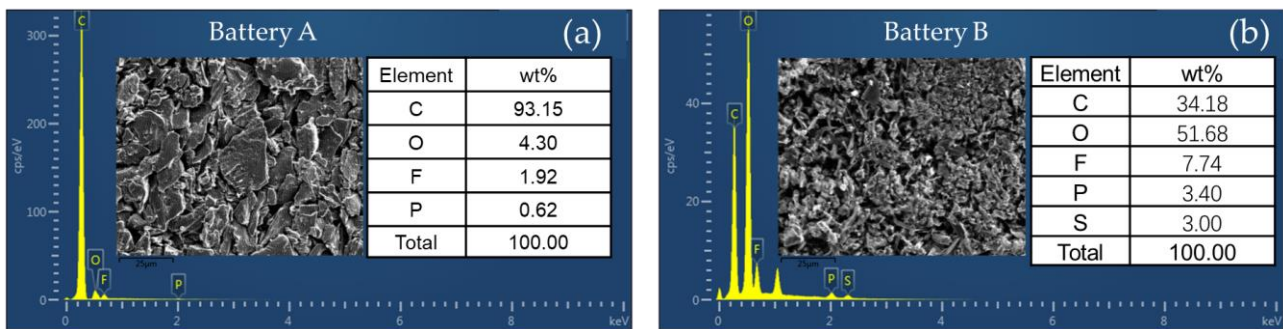


Figure 9. The EDS results of the negative electrode: (a) Battery A; (b) Battery B.

Consequently, by comparing the results of SEM and ESD of the two batteries, the operating parameter on the proposed operation boundary can effectively prevent lithium plating.

4.3.3. The Concern of the Battery Health

Apart from the risk of lithium plating, the potential side effects on the battery health are another concern for ACP. Hence, the tests, including EIS, RPT and ICA, were performed to explore the effect of the adopted current parameters stemming from the operation boundary on the battery health. The results are presented in Figure 10. The discharge capacity evolution of the two batteries is presented in Figure 10a. The discharge capacity of battery A is basically unchanged before and after the repeated preheating. In contrast, the discharge capacity of battery-B undergoes severe deterioration after repeat preheating of 800 cycles by 19.3%. The significant capacity degradation of battery B is highly related to lithium plating. On the one hand, the deposited Li metal can react with the electrolyte, forming a film of SEI. On the other hand, the deposited Li metal easily strips from the graphite surface and loses electrical contact with the negative electrode, then forming ‘dead Li’. Such two parasitic reactions jointly contribute to the capacity degradation of battery B. The different evolution in discharge capacity of the two batteries demonstrates the capability of the proposed operation boundary to avoid capacity degradation during ACP.

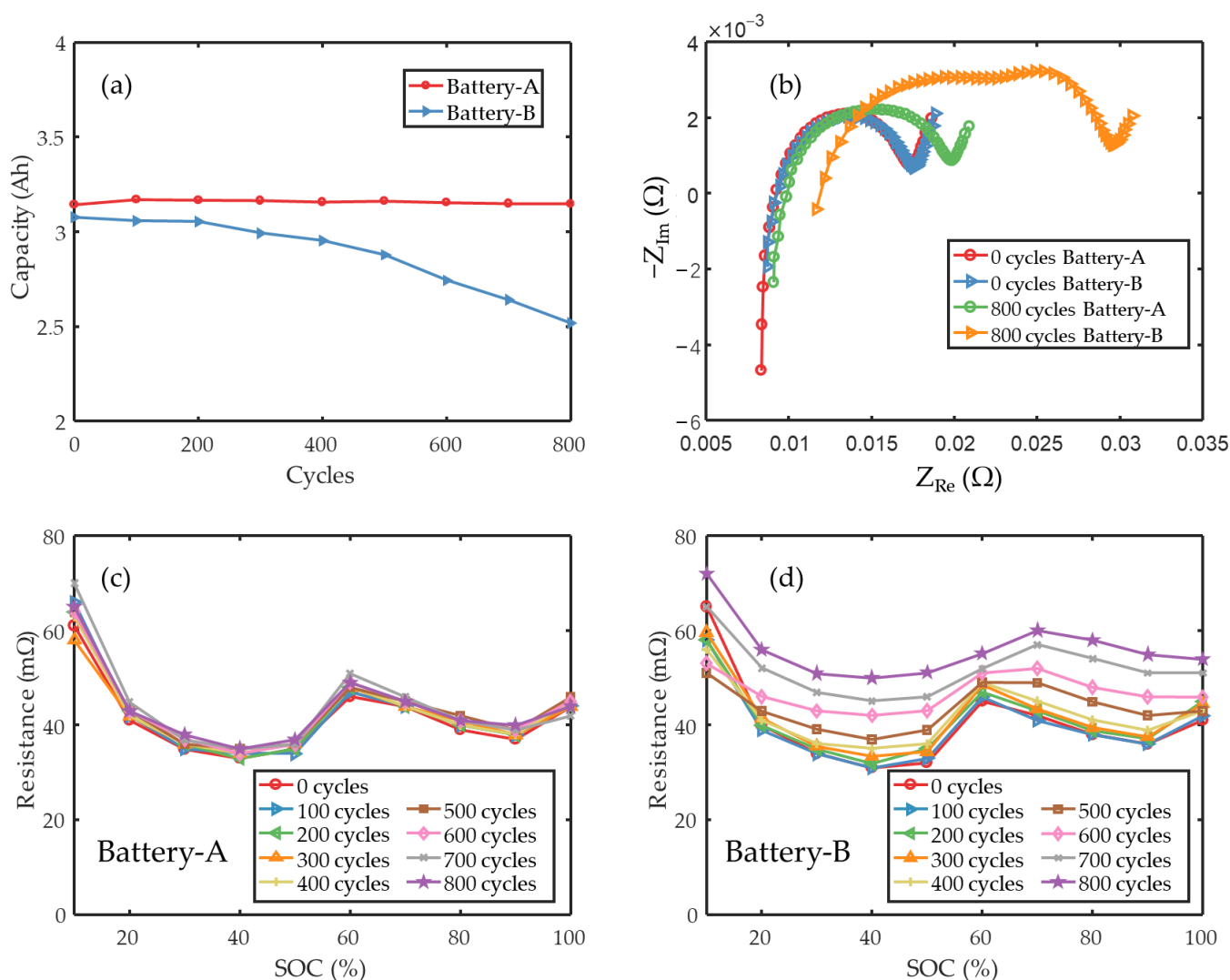


Figure 10. The evolution of (a) the discharge capacity, (b) the EIS at 50% SOC, (c,d) the direct current discharge resistance at 50% SOC.

The EIS of the two batteries were measured before and after the preheating cycles, and the results are presented in Figure 10b. Compared with battery A, the impedance of battery B in terms of R_o , R_{SEI} and R_{ct} increases a lot after the repeated preheating of 800 cycles. Regarding R_o (denoted by the real part impedance at $Z_{Im} = 0$), battery B noticeably increases since the consumption of the electrolyte caused by the formation of SEI on the deposited Li metal decreases the ionic conductivity of the electrolyte. Regarding R_{SEI} (characterized by the first semicircle at higher frequencies), the enlargement of battery B attributes the reason for the formation of SEI. Regarding R_{ct} (characterized by the second semicircle at low frequencies), the obvious increase in battery B is mainly because of the increased difficulties in the step of de-solvation of the solvated Li^+ in the electrolyte and in the step of transport of Li^+ in the SEI, which are considered to be caused by the consumption of the electrolyte and the increase in SEI [36]. In addition, compared with the EIS at the initial state, the two semicircles of EIS separate a little for battery B. It indicates the variation in the characteristic frequency of R_{SEI} and R_{ct} . Of note, as for battery A, the R_o , the R_{SEI} , and the R_{ct} also increase a little, possibly due to the formation of SEI and slight battery aging during repeat preheating.

As for the resistance in the time domain, 60 s of direct current discharge resistance was measured at different SOC so as to evaluate the power capability of the batteries. The

results are presented in Figure 10c,d. Similar to the impedance change in EIS, the resistance of battery B increases drastically with the increase in preheating cycles, while the resistance of battery A increases slightly. The reason for such a result is considered to be identical to that of impedance variation, as presented in Figure 10b.

To further identify the aging mechanism of repeated preheating, the incremental capacity (IC) is analyzed. The results are presented in Figure 11a,b. Consistent with the results of capacity and resistance/impedance variation, both the intensity of peaks and the shape of the IC signature exhibit noticeable changes for battery B. Specifically, the intensity of peak ① severely decreases after repeated preheating with the current amplitude out of the operation boundary. It implies the obvious loss of active material (LAM), which is induced by the electrode particle cracking or graphite exfoliation [37]. Both the IC signature and the intensity of peak ② cause severe change as well, demonstrating a pronounced loss of lithium inventory (LLI) caused by SEI formation and lithium plating [38]. In contrast, the IC curves of battery A vary little after repeated preheating tests, indicating a minimal detrimental effect on the battery lifetime.

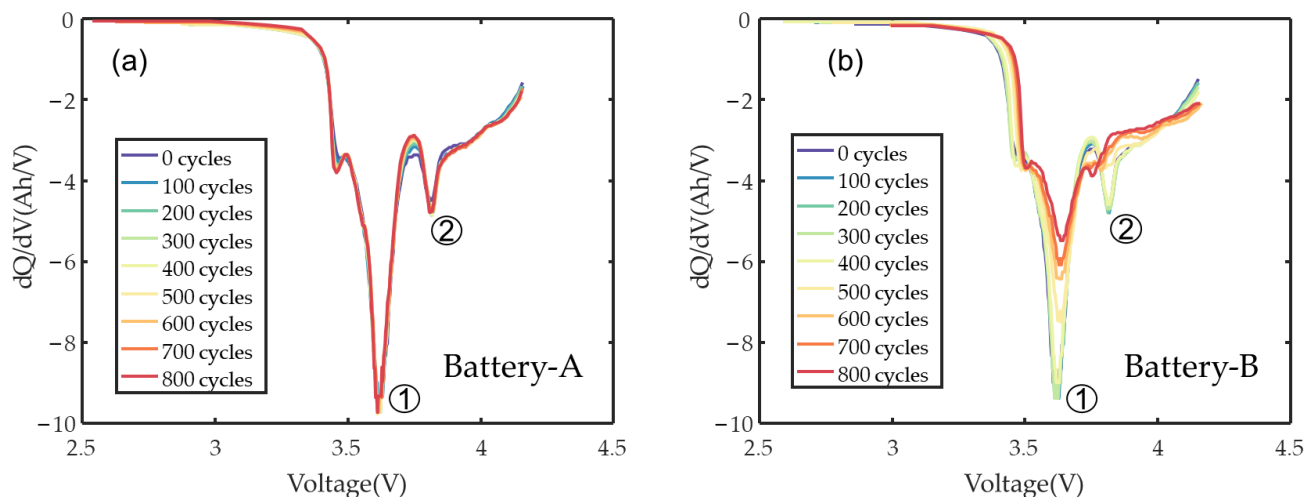


Figure 11. The evolution of the IC curves: (a) Battery A; (b) Battery B.

Considering the evolution of the discharge capacity, the resistance/impedance and the IC curves of battery A and battery B, the ACP with a square wave can effectively avoid battery degradation when the current parameter is on the proposed operation boundaries of lithium plating prevention. Certainly, it also applies to cases with the current parameters within the operation boundaries at a given temperature.

4.4. Temperature-Adaptive Preheating with SWAC

For a battery preheated at a fixed frequency, the battery temperature varies significantly during ACP, giving rise to a remarkable change in permissible current amplitude, as shown in Figure 6a. In such scenario, unchanged operating parameters would severely constrain the preheating capability. Consequently, an ACP method with a temperature-adaptive procedure is needed.

Figure 12a shows the maximum permissible current amplitudes at the frequencies of 100, 200, 300 and 400 Hz. The temperature ranges from -20 to 5 °C. The current amplitude is adjusted every battery temperature increase of 5 °C, i.e., the temperature interval equals 5 °C, and the processes are divided into five segments according to the measured EIS results. Due to the limitations of the current source, the ACP with a temperature-adaptive procedure is herein investigated by means of simulation. The temperature rising curves at different frequencies and thermal insulation conditions are presented in Figure 12b.

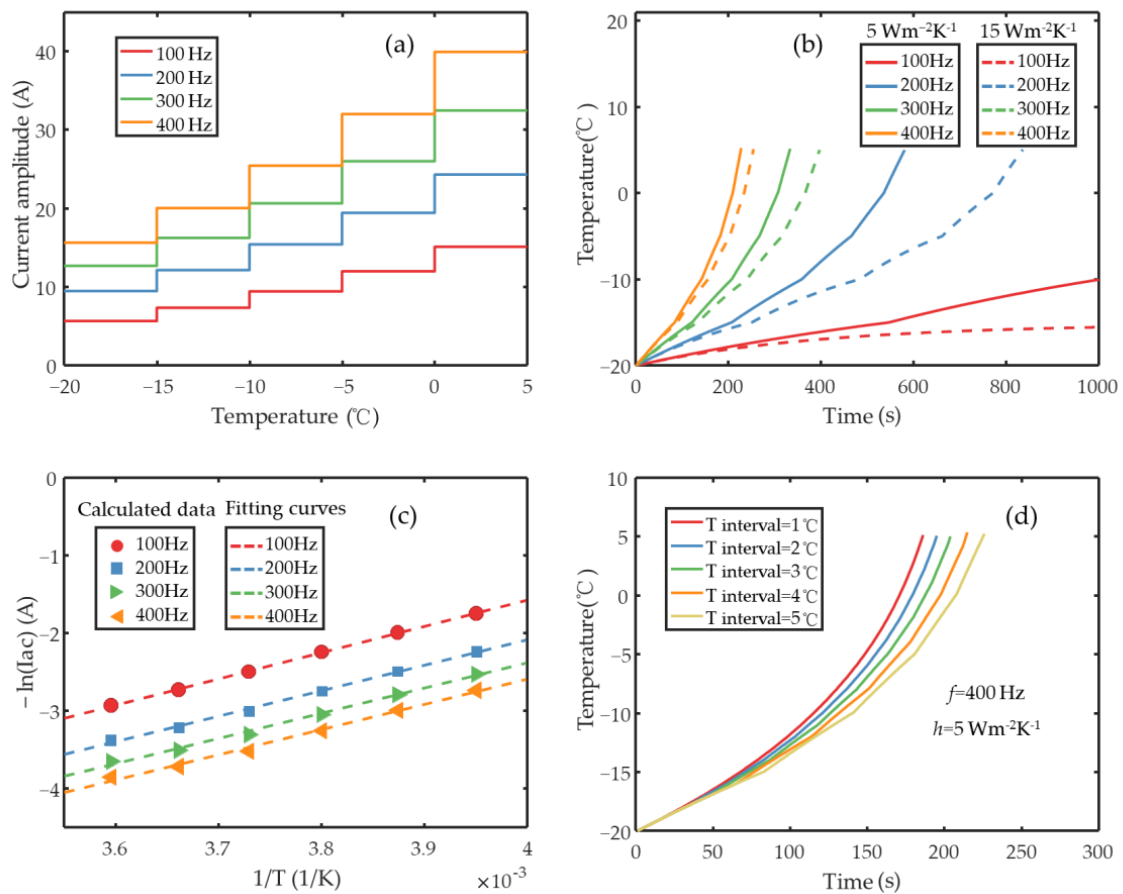


Figure 12. (a) The temperature-adaptive procedure at the frequencies of 100, 200, 300 and 400 Hz, the temperature interval is $5 \text{ }^\circ\text{C}$; (b) the temperature variation of the battery with the procedure as shown in Figure 12a and with heat transfer coefficients of 5 and $15 \text{ Wm}^{-2} \text{ K}^{-1}$; (c) the logarithm values and fitting lines of the maximum permissible current amplitudes I_{ac} at the frequencies of 100, 200, 300 and 400 Hz; (d) the temperature evolution of the battery with the temperature-adaptive procedure at the frequency 400 Hz, the heat transfer coefficient equals $5 \text{ Wm}^{-2} \text{ K}^{-1}$, the temperature intervals are 1, 2, 3, 4 and $5 \text{ }^\circ\text{C}$.

In the figure, the preheating rate varies a lot at different frequencies and thermal insulation conditions. Regarding the APC at a fixed thermal insulation condition, the preheating rate increases significantly at higher frequencies due to the larger permissible current amplitude. For example, when the battery is preheated at a frequency of 400 Hz and with a heat transfer coefficient of $5 \text{ Wm}^{-2} \text{ K}^{-1}$, the temperature rising rate can reach $6.61 \text{ }^\circ\text{C}/\text{min}$, capable of preheating the battery from -20 to $5 \text{ }^\circ\text{C}$ in 227 s. Regarding the APC at a fixed frequency, the preheating rate decreases at the thermal insulation condition with a larger heat transfer coefficient. For example, when the battery is preheated at a frequency of 200 Hz, the temperature rising rate with $5 \text{ Wm}^{-2} \text{ K}^{-1}$ is $2.59 \text{ }^\circ\text{C}/\text{min}$, while the temperature rising rate with $15 \text{ Wm}^{-2} \text{ K}^{-1}$ is $1.79 \text{ }^\circ\text{C}/\text{min}$. In addition, the difference in the preheating rate at the two thermal insulation conditions enlarges a lot at lower frequencies since the larger time consumption at lower frequencies increases the energy loss accumulated over time. Of note, as for the case at a frequency of 100 Hz, the battery fails to heat up to $5 \text{ }^\circ\text{C}$ within 800 s due to the low permissible current amplitude, as shown in Figure 12a.

The logarithm values of the maximum permissible current amplitudes I_{ac} at the frequencies of 100, 200, 300 and 400 Hz are presented in Figure 12c, where a good linear relationship with the inverse of the absolute temperature is found. The logarithm values of

I_{ac} at a fixed frequency are fitted using a linear function of $1/T$, as presented in Equation (20). The fitting results and quality are presented in Table 3.

$$-\ln(I_{ac}) = p_1 \frac{1}{T} + p_2 \quad (20)$$

Table 3. Fitting results and quality.

Frequency (Hz)	p ₁	p ₂	SEE
100	3378.2	−15.1	0.0003
200	3266.8	−15.2	0.0025
300	3240.9	−15.3	0.0047
400	3234.1	−15.5	0.0064

As shown in Figure 12c and Table 3, the maximum permissible current amplitudes at fixed frequencies are well-fitted by the linear functions with a tiny sum of squares error (SEE). It implies that the variation of the I_{ac} at a fixed frequency with temperature may follow the Arrhenius equation, which can greatly facilitate the acquirement of the maximum permissible amplitude at other temperatures.

Utilizing the fitting results, the paper further investigates the impact of the temperature interval in the procedure on the preheating rate at the frequency of 400 Hz and with the heat transfer coefficient of $5 \text{ Wm}^{-2} \text{ K}^{-1}$. The results with the temperature intervals of 1, 2, 3, 4 and 5 °C are presented in Figure 12d. From the figure, the temperature interval in the procedure has a significant effect on the preheating rate as well. When the temperature interval decreases to 1 °C, the temperature rising rate increases to 8.11 °C/min, and the battery can be heated up from −20 °C to 5 °C in 186 s.

In summary, many factors, such as the frequency (implying the maximum permissible current amplitude), thermal insulation condition and temperature interval of the temperature-adaptive procedure, significantly affect the preheating rate of the ACP method. Therefore, in order to increase the preheating rate, various factors need to be considered comprehensively.

4.5. Comparisons among the Preheating Methods Based on Different Control Strategies

As mentioned in Section 4.5, various factors, such as current parameters, thermal insulation condition, adopted temperature-adaptive procedure and even the used batteries, can significantly affect the preheating rate. Therefore, the preheating methods in previous works cannot make a simple comparison only in terms of preheating rate. To evaluate the method proposed in this paper more scientifically and rigorously, the other two methods based on the full-battery-based strategies, i.e., the full battery impedance control and the terminal voltage control, are implemented using the same battery parameters and under the identical thermal insulation condition.

Figure 13a–c shows the temperature variation of the battery preheated using the methods based on the full battery impedance control, the terminal voltage control and the anode potential control adopted in this paper. All three preheating methods adopt the temperature-adaptive procedure with the same temperature interval of 5 °C. The maximum permissible current amplitudes of adopting ACP methods based on two full-battery-based strategies are presented in the SM A3 and A4. The maximum permissible current amplitudes of using the method proposed in this paper are identical to the procedure shown in Figure 12a. The current of the three methods adopts the same square waveform. The heat transfer coefficient is $5 \text{ Wm}^{-2} \text{ K}^{-1}$. The frequencies are 200, 300 and 400 Hz, respectively. The preheating rate of using the three methods at different frequencies is presented in Figure 13d.

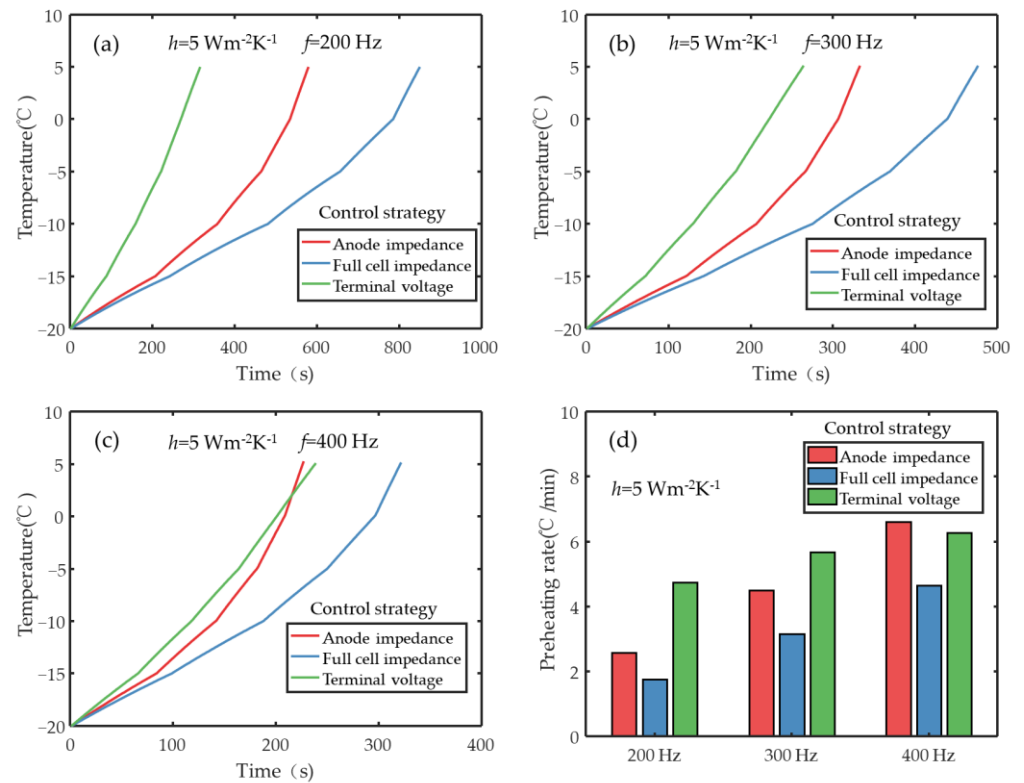


Figure 13. The temperature evolution and the preheating rate of the battery preheated using the methods based on different control strategies; (a) the preheating is at the frequency of 200 Hz; (b) the preheating is at the frequency of 300 Hz; (c) the preheating is at the frequency of 400 Hz; (d) the preheating rate of the battery preheated using the methods based on different control strategies, the heat transfer coefficient equals $5 \text{ Wm}^{-2} \text{ K}^{-1}$.

Regarding the preheating based on the full battery impedance control strategy, the preheating rate at all the frequencies is lower than that of the proposed method in this paper. Moreover, the weakness becomes more pronounced at a higher frequency. For example, when the battery is preheated at a frequency of 400 Hz, the preheating rate of the method proposed in this paper reaches $6.61 \text{ }^\circ\text{C}/\text{min}$ and is larger than that based on the full battery impedance control strategy by 41.8%. The reason for such result is mainly because of the introduced safety threshold when employing the full battery impedance instead of the negative electrode impedance [16].

Regarding the preheating method based on the terminal voltage control strategy, despite the fact that its preheating rate is the fastest among the three methods at frequencies of 200 and 300 Hz, the strength fades significantly with increasing the frequency. When the frequency reaches 400 Hz, the preheating rate becomes lower than that of the method proposed in this paper by 5.4%. In addition, as shown in Figure 14, the $|V_3^{\text{neg}}|$, which is calculated using Equation (19), exceeds the U_e in the preheating process of using the method based on the terminal voltage control. The result indicates the method based on the terminal voltage control can lead to lithium plating at selected frequencies. Consequently, considering the preheating rate and the lithium plating prevention, the method proposed in the paper can maximize the preheating rate and ensure no lithium plating during the preheating. In particular, the method shows more robust strength at high frequency than the methods based on the two full-battery-based strategies.

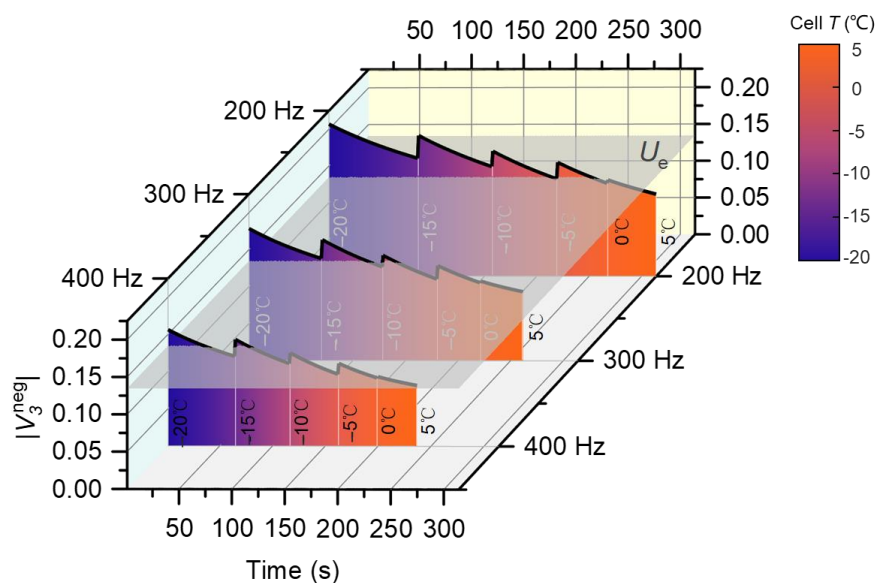


Figure 14. The variation in $|V_3^{\text{neg}}|$ in the preheating process of using the method based on the terminal voltage control. The frequencies are 200, 300 and 400 Hz, the preheating adopts the temperature-adaptive procedure with the temperature interval of $5\text{ }^\circ\text{C}$, and the maximum permissible current amplitudes are presented in Supplementary Figure S4b.

5. Conclusions

In this paper, a rapid preheating method capable of preventing lithium plating was developed using a square wave alternating current. The method achieves a higher preheating capability, capable of warming up the battery faster than that with sinusoidal alternating current. The strategy of anode potential control is adopted to maximize the preheating rate. Operation boundaries of lithium plating prevention, in terms of frequency and maximum permissible current amplitude, are determined using the anode impedance and potential. The effectiveness in preventing lithium plating, together with its influence on battery health, is experimentally investigated. After repeated preheating of 800 cycles at $-20\text{ }^\circ\text{C}$, no lithium plating is observed on the graphite electrode, and negligible effect on battery degradation is confirmed.

By integrating the operation boundaries and the square wave preheating method, a temperature-adaptive amplitude procedure with different control parameters is explored. The procedure is found to be able to significantly speed up the preheating rate with higher frequency, smaller temperature intervals, and better thermal insulation. Another two methods based on the full battery impedance control and the terminal voltage control are implemented. The results demonstrate that the proposed method in this paper has a larger preheating rate than these using the full-battery-based strategies at high frequency. When the battery is preheated at a frequency of 400 Hz, with a temperature interval of $5\text{ }^\circ\text{C}$ and a heat transfer coefficient of $5\text{ Wm}^{-2}\text{ K}^{-1}$, the preheating rate can reach $6.61\text{ }^\circ\text{C}/\text{min}$, exceeding the method based on the terminal voltage control by 5.4%, and larger than that based on the full battery impedance control strategy by 41.8%.

In extending the method to the battery module or pack, despite the fact that several excellent works have provided implementation schemes in terms of hardware circuits, the effect of the battery-to-battery variations on the uniformity in terms of temperature and operation boundaries of lithium plating prevention has not been considered yet. The related work will be carried out in a future study so as to revise the operation boundaries and improve the robustness of the proposed method for practical applications.

Supplementary Materials: The following supporting information can be downloaded at: <https://www.mdpi.com/article/10.3390/pr11041089/s1>, Figure S1. The validation of the effectiveness of the reference electrode. (a) The EIS of the positive electrode, the EIS of the negative electrode and the EIS of the full cell at 50% SOC; (b) The OCV change of each electrode at different SOC; Figure S2. The cell temperature T , $\ln(T - T_{amb})$ and the calibrated equivalent heat transfer coefficient h with time during cooling: (a) Cell temperature T ; (b) The value of $\ln(T - T_{amb})$ and the calibrated equivalent heat transfer coefficient h ; Figure S3. (a) Operation boundaries for preventing lithium deposition calculated using the full cell impedance; (b) The temperature-adaptive procedure for the method based on the full cell impedance control strategy, the frequency is 200 Hz, 300 Hz and 400 Hz, the temperature interval is 5 °C; Figure S4. (a) Operation boundaries for preventing lithium deposition based on the terminal voltage control; (b) The temperature-adaptive procedure for the method based on the terminal voltage control strategy, the frequency is 200 Hz, 300 Hz and 400 Hz, the temperature interval is 5 °C.

Author Contributions: G.L., conceptualization, investigation, writing—review and editing, visualization, funding acquisition. Z.Z., conceptualization, formal analysis, methodology, writing—original draft, writing—review and editing, visualization. J.G., conceptualization, writing—review and editing. Q.L., writing—review and editing. Y.Z., writing—review and editing. H.Z., writing—review and editing. All authors have read and agreed to the published version of the manuscript.

Funding: This research was funded by the Natural Science Foundation of Hunan Province, China (grant number 2021JJ60030).

Data Availability Statement: The data presented in this study are available on request from the corresponding author.

Conflicts of Interest: The authors declare that they have no known competing financial interests or personal relationships that could have appeared to influence the work reported in this paper.

Nomenclature

A	period of alternating current (s)
c	specific heat capacity ($J \cdot g^{-1} \cdot K^{-1}$)
h	heat transfer coefficient ($W \cdot m^{-2} \cdot K^{-1}$)
i	alternating current (A)
I	charge/discharge current (A)
I_{ac}	amplitude of alternating current (A)
m	cell mass (kg)
n_{SEI}	exponent of constant phase element
n_{dl}	exponent of constant phase element
q	heat generation rate (W)
Q_{SEI}	coefficient of constant phase element
Q_{dl}	coefficient of constant phase element
R_o	ohmic resistance (Ω)
R_{SEI}	solid electrolyte interphase resistance (Ω)
R_{ct}	charge transfer resistance (Ω)
S	surface area of the cell (m^2)
t	time (s)
T	cell temperature (K)
T_{amb}	ambient temperature (K)
U_{oc}	open-circuit voltage (V)
U_e	equilibrium potential (V)
U_n	voltage (V)
V	terminal voltage (V)
V_3	voltage across charge transfer resistance of negative electrode (V)
Z_{Re}	real part of impedance (Ω)
Z_3	impedance of charge transfer of negative electrode (Ω)
ω	angular frequency ($rad \cdot s^{-1}$)
η	over-potential of anode electrode (V)
φ	phase angle of impedance (rad)
Φ	potential (V)

Superscript or Superscript

<i>l</i>	liquid phase
neg	negative electrode
pos	positive electrode
s	solid phase
SAC	sinusoidal alternating current
SWAC	square wave alternating current

Abbreviations

ACP	alternating current preheating
CPE	constant phase element
EIS	electrochemical impedance spectroscopy
EEC	equivalent electrical circuit
EDS	energy-dispersive X-ray spectroscopy
ICA	incremental capacity analysis
IC	incremental capacity
LIB	lithium-ion battery
NR _{ct}	charge transfer impedance of negative electrode
OCV	open-circuit voltage
PR _{ct}	charge transfer impedance of positive electrode
RPT	reference performance test
SOC	state of charge
SEI	solid electrolyte interphase
SEM	scanning electron microscope
SEE	sum of squares due to error
SAC	sinusoidal alternating current
SWAC	square wave alternating current

References

- Ge, H.; Aoki, T.; Ikeda, N.; Suga, S.; Isobe, T.; Li, Z.; Tabuchi, Y.; Zhang, J. Investigating Lithium Plating in Lithium-Ion Batteries at Low Temperatures Using Electrochemical Model with NMR Assisted Parameterization. *J. Electrochem. Soc.* **2017**, *164*, A1050–A1060. [[CrossRef](#)]
- Li, Z.; Huang, J.; Liaw, B.Y.; Metzler, V.; Zhang, J. A review of lithium deposition in lithium-ion and lithium metal secondary batteries. *J. Power Sources* **2014**, *254*, 168–182. [[CrossRef](#)]
- Wang, F.; Zhang, J.; Wang, L. Design of electric air-heated box for batteries in electric vehicles. *Chin. J. Power Sources* **2013**, *37*, 1184–1187. (In Chinese)
- Luo, Y.; Lang, C.; Luo, P. Study on heating system of lithium ion battery at low temperature. *J. South China Univ. Technol.* **2016**, *44*, 100–106. (In Chinese)
- Li, G.; Huang, X.; Fu, X.; Yang, Y. Design research on battery heating and preservation system based on liquid cooling mode. *J. Hunan Univ.* **2017**, *44*, 26–33. (In Chinese)
- Zhang, J.; Ge, H.; Li, Z.; Ding, Z. Internal heating of lithium-ion batteries using alternating current based on the heat generation model in frequency domain. *J. Power Sources* **2015**, *273*, 1030–1037. [[CrossRef](#)]
- Zhu, J.G.; Sun, Z.C.; Wei, X.Z.; Dai, H.F.; Gu, W.J. Experimental investigations of an AC pulse heating method for vehicular high power lithium-ion batteries at subzero temperatures. *J. Power Sources* **2017**, *367*, 145–157. [[CrossRef](#)]
- Jiang, J.; Ruan, H.; Sun, B.; Wang, L.; Gao, W.; Zhang, W. A low-temperature internal heating strategy without lifetime reduction for large-size automotive lithium-ion battery pack. *Appl. Energy* **2018**, *230*, 257–266. [[CrossRef](#)]
- Shang, Y.; Zhu, C.; Lu, G.; Zhang, Q.; Cui, N.; Zhang, C. Modeling and analysis of high-frequency alternating-current heating for lithium-ion batteries under low-temperature operations. *J. Power Sources* **2020**, *450*, 227435. [[CrossRef](#)]
- Li, Y.; Gao, X.; Qin, Y.; Du, J.; Guo, D.; Feng, X.; Lu, L.; Han, X.; Ouyang, M. Drive circuitry of an electric vehicle enabling rapid heating of the battery pack at low temperatures. *iScience* **2021**, *24*, 101921. [[CrossRef](#)]
- Ge, H.; Huang, J.; Zhang, J.; Li, Z. Temperature-Adaptive Alternating Current Preheating of Lithium-Ion Batteries with Lithium Deposition Prevention. *J. Electrochem. Soc.* **2015**, *163*, A290–A299. [[CrossRef](#)]
- Wu, X.; Cui, Z.; Chen, E.; Du, J. Capacity degradation minimization oriented optimization for the pulse preheating of lithium-ion batteries under low temperature. *J. Energy Storage* **2020**, *31*, 101746. [[CrossRef](#)]
- Ruan, H.; Jiang, J.; Sun, B.; Zhang, W.; Gao, W.; Wang, L.Y.; Ma, Z. A rapid low-temperature internal heating strategy with optimal frequency based on constant polarization voltage for lithium-ion batteries. *Appl. Energy* **2016**, *177*, 771–782. [[CrossRef](#)]

14. Zhu, J.; Sun, Z.; Wei, X.; Dai, H. An alternating current heating method for lithium-ion batteries from subzero temperatures. *Int. J. Energy Res.* **2016**, *40*, 1869–1883. [[CrossRef](#)]
15. Guo, S.; Xiong, R.; Wang, K.; Sun, F. A novel echelon internal heating strategy of cold batteries for all-climate electric vehicles application. *Appl. Energy* **2018**, *219*, 256–263. [[CrossRef](#)]
16. Jian, J.; Zhang, Z.; Wang, S.; Gong, J. Analysis of control strategies in alternating current preheating of lithium-ion cell. *Appl. Energy* **2023**, *333*, 120533. [[CrossRef](#)]
17. Li, Y.; Han, X.; Feng, X.; Chu, Z.; Gao, X.; Li, R.; Du, J.; Lu, L.; Ouyang, M. Errors in the reference electrode measurements in real lithium-ion batteries. *J. Power Sources* **2021**, *481*, 228933. [[CrossRef](#)]
18. Chu, Z.; Feng, X.; Liaw, B.; Li, Y.; Lu, L.; Li, J.; Han, X.; Ouyang, M. Testing Lithium-Ion Battery with the Internal Reference Electrode: An Insight into the Blocking Effect. *J. Electrochem. Soc.* **2018**, *165*, A3240–A3248. [[CrossRef](#)]
19. Raccichini, R.; Amores, M.; Hinds, G. Critical Review of the Use of Reference Electrodes in Li-Ion Batteries: A Diagnostic Perspective. *Batteries* **2019**, *5*, 12. [[CrossRef](#)]
20. Timmons, A.T.; Verbrugge, M.W. Lithium-Ion Cell with an Array of Reference Electrodes. U.S. Patent 8,586,222 B2, 8 April 2010.
21. Wang, S.; Wang, J.; Soukiazian, S.; Sherman, E. U.S. Patent 9,847,558 B1, 10 October 2014.
22. Wijayawardhana, C.; Neumann, G.; Gulde, P. U.S. Patent 2013/0323542 A1, 12 October 2011.
23. Liu, J.; Han, X.; Chu, Z.; Lu, L.; Ouyang, M.; Zheng, Y. China Patent CN 110702751 A, 17 January 2020.
24. Gordon, I.J.; Grugeon, S.; Débart, A.; Pascaly, G.; Laruelle, S. Electrode contributions to the impedance of a high-energy density Li-ion cell designed for EV applications. *Solid State Ion.* **2013**, *237*, 50–55. [[CrossRef](#)]
25. Qu, Z.G.; Jiang, Z.Y.; Wang, Q. Experimental study on pulse self-heating of lithium-ion battery at low temperature. *Int. J. Heat Mass Transf.* **2019**, *135*, 696–705. [[CrossRef](#)]
26. Qin, Y.; Du, J.; Lu, L.; Gao, M.; Haase, F.; Li, J.; Ouyang, M. A rapid lithium-ion battery heating method based on bidirectional pulsed current: Heating effect and impact on battery life. *Appl. Energy* **2020**, *280*, 115957. [[CrossRef](#)]
27. Wu, B.; Li, Z.; Zhang, J. Thermal Design for the Pouch-Type Large-Format Lithium-Ion Batteries. *J. Electrochem. Soc.* **2014**, *162*, A181–A191. [[CrossRef](#)]
28. Zhang, J.; Huang, J.; Li, Z.; Wu, B.; Nie, Z.; Sun, Y.; An, F.; Wu, N. Comparison and validation of methods for estimating heat generation rate of large-format lithium-ion batteries. *J. Therm. Anal. Calorim.* **2014**, *117*, 447–461. [[CrossRef](#)]
29. Zhang, G.; Cao, L.; Ge, S.; Wang, C.-Y.; Shaffer, C.E.; Rahn, C.D. In situ measurement of radial temperature distributions in cylindrical Li ion cells. *J. Electrochem. Soc.* **2014**, *161*, A1499. [[CrossRef](#)]
30. Petzl, M.; Danzer, M.A. Nondestructive detection, characterization, and quantification of lithium plating in commercial lithium-ion batteries. *J. Power Sources* **2014**, *254*, 80–87. [[CrossRef](#)]
31. Legrand, N.; Knosp, B.; Desprez, P.; Lapique, F.; Raël, S. Physical characterization of the charging process of a Li-ion battery and prediction of Li plating by electrochemical modelling. *J. Power Sources* **2014**, *245*, 208–216. [[CrossRef](#)]
32. Tippmann, S.; Walper, D.; Balboa, L.; Spier, B.; Bessler, W.G. Low-temperature charging of lithium-ion cells part I: Electrochemical modeling and experimental investigation of degradation behavior. *J. Power Sources* **2014**, *252*, 305–316. [[CrossRef](#)]
33. Meyers, J.P.; Doyle, M.; Darling, R.M.; Newman, J. The impedance response of a porous electrode composed of intercalation particles. *J. Electrochem. Soc.* **2000**, *147*, 2930. [[CrossRef](#)]
34. Wang, Z.; Li, Z.; Huang, J.; Zhang, J. Formation of a lithium-plated reference electrode in lithium-ion cells: Characterization using dynamic impedance and simulation using electrochemical model. *ECS Trans.* **2017**, *75*, 151. [[CrossRef](#)]
35. Zhang, Z.; Li, Z.; Yang, X.; Gong, J.; Zhang, J. Thermal management of parallel cells—Methodology based on non-linear dynamics. *eTransportation* **2022**, *13*, 100181. [[CrossRef](#)]
36. Jow, T.R.; Delp, S.A.; Allen, J.L.; Jones, J.-P.; Smart, M.C. Factors Limiting Li+Charge Transfer Kinetics in Li-Ion Batteries. *J. Electrochem. Soc.* **2018**, *165*, A361–A367. [[CrossRef](#)]
37. Dubarry, M.; Dubarry, M.; Svoboda, V.; Hwu, R.; Liaw, B.Y. Incremental capacity analysis and close-to-equilibrium OCV measurements to quantify capacity fade in commercial rechargeable lithium batteries. *Electrochem. Solid State Lett.* **2006**, *9*, A454. [[CrossRef](#)]
38. Waldmann, T.; Hogg, B.-I.; Wohlfahrt-Mehrens, M. Li plating as unwanted side reaction in commercial Li-ion cells—A review. *J. Power Sources* **2018**, *384*, 107–124. [[CrossRef](#)]

Disclaimer/Publisher’s Note: The statements, opinions and data contained in all publications are solely those of the individual author(s) and contributor(s) and not of MDPI and/or the editor(s). MDPI and/or the editor(s) disclaim responsibility for any injury to people or property resulting from any ideas, methods, instructions or products referred to in the content.